Results in Materials 16 (2022) 100341

Contents lists available at ScienceDirect

Results in Materials

journal homepage: www.sciencedirect.com/journal/results-in-materials

Directed energy deposition of AA7075 - Effect of TiC nanoparticles on microstructure

Lucia Cobian Gonzalez, Jari Tuominen *, Shahroz Ahmed, Madan Patnamsetty, Pasi Peura

Tampere University, Materials Science and Environmental Engineering, FI-33720 Tampere, Finland

ARTICLE INFO

Keywords:
AA7075
Laser-DED
Nucleation enhancers
Post-heat treatment
Microstructure

ABSTRACT

AA7075 alloy is a high-strength aluminum alloy with properties enhanced by heat treatments. However, like most high-strength aluminum alloys, AA7075 is non-weldable, as it suffers from hot cracking when it is welded or additively manufactured with fusion techniques. A proposed way to reduce the hot cracking tendency is by refining the microstructure by adding nucleation enhancers. In this study, AA7075 powder feedstock was functionalized with 1.7 and 3.4 vol% TiC nanoparticles, printed with laser-directed energy deposition (DED), subjected to T6 heat treatment, and characterized with optical and electron microscopy, electron backscatter diffraction (EBSD), and hardness measurements. Although TiC was not homogeneously distributed in the aluminum matrix, the addition of TiC successfully suppressed hot cracking by inhibiting dendritic growth produced by increased and more uniform nucleation, which resulted in refined equiaxed grains, and thus enhanced the printability of the material.

1. Introduction

The interest in additive manufacturing (AM) for industrial applications has been increasing in recent years due to the fast transformation from prototyping to manufacturing applications. Another feature of this technology that the industry is interested in is that it has the potential to repair and manufacture components of complex geometries that cannot be obtained through conventional manufacturing processes [1]. Directed energy deposition (DED) is an AM technique that can produce high dimension components and add features to existing geometries within a short period.

AA7075 is one of the most commonly used aluminum alloys in industry, especially in aerospace, as it has high mechanical strength, corrosion resistance, and reasonable machinability. In addition, heat treatments can further enhance its mechanical properties. From the AM point of view, it has been considered non-weldable. The main problem of AA7075 is that it suffers from hot cracking when it is 3D printed and welded; in other words, cracks appear in the rapidly solidified metal, which risks the component's structural integrity [2,3]. Besides cracks, porosity and embedded alumina foils are other common problems when welding high-strength aluminum alloys. Pores originate as a result of gas entrapment during solidification. The main gas that causes porosity is hydrogen, which has a high solubility in molten metals but decreases as the material solidifies, becoming entrapped inside. Hydrogen during welding can come from moisture, flux, or the gas supply that prevents oxidation if damaged [4]. In AM, porosity can also be caused by low boiling point alloying elements, such as Mg and Zn, as the gas becomes entrapped in solid due to the rapid cooling rates [2]. The size of the pores can go from micrometric to millimetric [4].

Hot cracking is a high-temperature cracking mechanism that occurs on certain alloys containing phases with melting points considerably lower than the solvent or rejected atoms. When the material cools down, the material with less alloying elements solidify as nuclei, where other atoms attach and grow creating dendrites. While dendrites grow, they push lower melting phases and other alloying elements towards the interdendritic space, where they accumulate causing segregation. Upon growth, they finally collide with other ones, creating boundaries. As a result, the remaining melt becomes entrapped between the long channels that form the boundaries. As the material cools down, the remaining molten material solidifies and contracts, applying strain and creating cracks [4].

There are several solutions to reduce the probability of hot cracking. For example, high welding speeds reduce the heat-affected zone (HAZ) depth and cooling time reducing the shrinkage stresses. In general, the used welding methods are the ones that reduce the internal stresses or use an appropriate filler that has a narrow range between liquidus and

* Corresponding author.
E-mail address: jari.tuominen@tuni.fi (J. Tuominen).

https://doi.org/10.1016/j.rinma.2022.100341
Received 27 July 2022; Received in revised form 16 October 2022; Accepted 19 October 2022
Available online 28 October 2022

solidus lines, i.e. a narrow mushy area [4].

Another solution for hot cracking is to refine the microstructure. This refinement is achieved by functionalizing the alloy with nanoparticles that act as nucleation enhancers. These nanoparticles should have matching crystallographic lattice spacing and density providing a low-energy nucleation barrier [5]. The presence of nucleation enhancers reduces dendritic growth and encourages heterogeneous nucleation [6–8]. As a result, the microstructure shows refined equiaxed grains. With this heterogeneous nucleation, dendrite growth is limited, avoiding entrapment of the liquid phases between the interdendritic space and later cracking. Titanium, zirconium, and scandium nanocomposites are used for grain refinement [4,7,8].

AA7075 is a high-strength alloy whose mechanical properties can be enhanced with T6 heat treatment due to its alloying elements. Alloying elements, however, generate a large mushy area during solidification, which increases the tendency for hot cracking [2,3]. AA7075 has a solidification range of more than 100 °C from the most abundant element, Al (T_m 660 °C), to the main alloy element, which is Zinc (T_m 420 °C) [9]. Besides, phase S' Al_2CuMg (T_m 490 °C) has a lower melting point than its constituents. Liquid material becomes entrapped between the interdendritic space, which later solidifies and contracts, creating strains that tear off the material, producing cracks. According to Bhagavatam [3,6], "during welding of Al 7075, hot cracking may occur due to the liquation of Al_2CuMg and Fe-rich particles surrounded with Cu_2FeAl within the solid solubility limit due to the high cooling rate."

One solution to this problem is to nanofunctionalize the alloy with nucleation enhancers. There have been studies of grain refinement of aluminum alloys with nucleation enhancers since the 1950s. Results indicated that adding small amounts of W, Ti, Zr, B, and Cr acted as nuclei for an effective grain refinement [10]. There have been studies with successful grain refinement with pure elements Sc, Zr, and Ti alone or combined [11]. Since the mid-2010s, there have been studies for aluminum castings of the 2xxx and 7xxx series, with Al_2O_3, SiC, TiC, Ag, and Sn nano compounds, including 7075 castings [12–17].

The studies of nucleation enhancers in welding have started recently, with most of the investigations considering 7075 published in the past few years. For welding 7075, the most used nanoparticles are Ti and Zr compounds [6,18]. Embedding TiC nanoparticles in welding wires has also suppressed hot cracking [6,19].

In parallel to solve hot cracking in 7075 aluminum alloy during welding, there have been studies on how to work with 7075 when using AM methods. Most publications concern powder bed fusion (PBF), where researchers try to solve hot cracking by adding TiB_2, TiC, Sc, and Zr compound nanoparticles as nucleation enhancers [20,21].

Although hot cracking has been solved in welding applications and is being explored with PBF, there is no detailed information on the use of nucleation enhancers in laser DED of AA7075 alloy and its response to thermal post-processing.

2. Materials and methods

2.1. Powders

The AA7075 powder feedstock consisted of spherical particles with sizes in the range of 50–150 μm (TLS Technik GmbH & Co. Spezialpulver KG, Bitterfeld-Wolfen, Germany), Fig. 1. The composition given by the feedstock supplier is shown in Table 1, which conforms with the EN 573–3:2019 standard. SEM micrographs illustrate spherical particles with an average size of around 60 μm, obtained with the help of ImageJ (NIH and LOCI, University of Wisconsin, USA).

Aluminum powder was functionalized with TiC nanoparticles of 50 nm in diameter (Hunan Huawei Jingcheng Material Technology Co., Changsa, China) displayed in Fig. 1b. Two powder mixtures were prepared, one with a concentration of 1.7 and the other with 3.4 vol% of TiC. The selected concentrations, 1.7% and 3.4%, are based on the work of Sokoluk et al., where it was studied how welding rods modified with 1.7% vol. of TiC nanoparticles suppressed hot cracking and modified the grain structure of AA7075 during arc welding [6].

After weighing the components of the mixes, they were blended by ball milling to get a homogeneous mixture. Ball milling was employed to attach the nanoparticles to the aluminum powder to enhance the flowability. The mixing was performed with a Fritsch Pulverisette 5 planetary mill (FRITSCH, Idar-Oberstein, Germany) at 200RPM for 3 h. A 4:1 wt ratio of steel balls of 10 mm in diameter was used for the milling process. The mixtures were sieved with a mesh size of 150 μm due to the maximum particle size of the powder-feeding nozzle.

2.2. Laser DED

The DED system set-up comprised four main equipment components; laser, coaxial powder nozzle, powder feeder, and a kinematic robot. The laser was a CORELASE 3 kW fiber laser (Coherent Inc. Santa Clara, USA) of 400 μm fiber diameter, with an f120 collimator and f250 optics. The laser beam was ejected through the center of a Coax 8 powder nozzle (Fraunhofer IWS, Dresden, Germany). The powders were fed by a Medicoat Duo powder feeder (Medicoat AG, Mägenwil, Switzerland). The powders were deposited on the 8 mm thick plates made from the weldable AA5754 with temper H111 (EN AW-5754-H111), which were clamped to a processing table of Fanuc F-200iB parallel kinematic robot (Fanuc Ltd., Oshino, Japan). Table 2 and Fig. 2a show the process parameters and system set-up. Fig. 2b summarizes the experimental procedure consisting of single walls.

Table 1
Chemical composition of AA7075 powder (wt.%).

Al	Zn	Mg	Cu	Fe	Si	Mn	Cr	Ti
Bal.	5.22	2.46	1.46	0.13	0.35	0.17	0.24	0.16

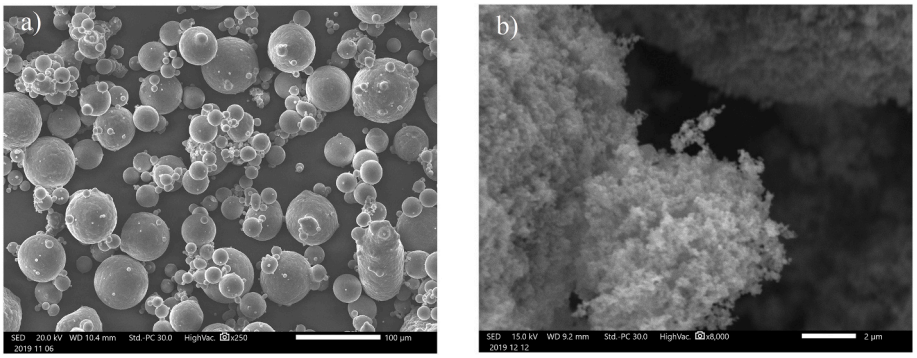

Fig. 1. SEM micrograph of a) AA7075 powder and b) TiC nanoparticles.

Table 2
Laser DED process parameters.

Parameter	Value
Power	1000 W
Spot ⌀	2.5 mm
Travel speed (TS)	8.3–16.7 mm/s
Powder feed rate (PFR)	1.6–3.2 g/min
Carrier gas flow (Ar)	6 l/min
Shielding gas flow (Ar)	15 l/min
Number of layers	10 and 50
Layer height (LH)	0.1–0.2 mm
Interpass time	1 s
Preheat	RT, 260 °C
Powders	AA7075, AA7075 + TiC

2.3. Thermal post-processing

Part of the samples was heat-treated to the T6 temper (Table 3). This heat treatment consists of two steps, solution annealing and precipitation hardening. First, the samples were solution treated at 480 °C for 50 min and quenched in room temperature (RT) water just after extraction from the oven to avoid precipitation. According to JMatPro simulations, $MgZn_2$ starts to precipitate at around 340 °C after 4 s, so the cooling rate must be high, at least 100 °C/s. A CCT diagram obtained with JMatPro is shown in Fig. 3a.

After quenching the samples, they were precipitation hardened at 120 °C for 21 and 24 h to determine the time for the maximum strength. Fig. 3b depicts the precipitation sequence as a function of time. During the first minute, there is a rapid increase in the formation of GP until it stabilizes at around 2%. After 1 h, GP zones grow and transform into T′ and η′, where η′ gives the maximum hardening effect. This is explained by the GP content decrease and the increment of T′ and η′ precipitates after 1 h. After 20 h, precipitation of these two phases stops, as its At.% stabilizes, while S′ and θ' phases start to precipitate.

2.4. Characterization

The microstructure was analyzed using an optical microscope Leica DM2500 M (Leica Microsystems GmbH, Wetzlar, Germany), JEOL JSM-IT500 (Jeol Ltd., Tokyo, Japan) SEM equipped with an EDS detector. For EBSD analysis, the Zeiss ULTRAplus SEM (Carl Zeiss AG, Oberkochen, Germany) was equipped with Oxford Instruments Symmetry CMOS EBSD detector. It was operated at an accelerating voltage of 15 kV and a step size of 1 μm for 500 × 500 μm scanning areas and 4.9 μm for 2300 × 2600 μm scanning area. In addition, grains with more than 15° boundary misorientation angle and grains with more than 10 pixels were considered.

Hardness was measured using microhardness tester Matsuzawa MMT-X7 (Matsuzawa Co., Ltd, Akita, Japan), which measures the Vickers hardness of the samples with a 200 g load. Hardness was analyzed the entire sample, from top to bottom, by successive vertical measurements separated around 0.5 mm from each other and starting 0.1 mm below the top of the sample.

3. Results and discussion

3.1. Microstructure analysis

Fig. 4 shows four samples made with the optimum fabrication parameters. Samples a and b were made of pure AA7075 powder. In Fig. 4a, the base plate was at RT and 4b at 260 °C. Fig. 4c and d presents samples with different TiC concentrations, 1.7% and 3.4%, respectively.

Both a and b samples (non-functionalized) presented cracks in the building direction, but the area on the top contained none. The sample made with a preheated plate also exhibits dark bands that indicate a layered structure. These dark bands may be the result of over-etching. The origin of the layered structure will be explained later.

Fig. 5 displays the microstructures of the samples at a higher magnification. Fig. 5b and d (made with non-functionalized powder) show cracks oriented towards the building direction, and in the space between the cracks, small voids that are equidistant in the direction perpendicular to the building one and linearly displaced in the building direction. These voids are probably the result of isolated liquid pockets that remain after dendrites' secondary branches coalesce [22].

The top area of samples made with non-functionalized powders, which are illustrated in Fig. 5a and c, present grains with a dendritic structure oriented in different directions. The sample fabricated on a preheated plate has coarse dendrites that exhibit secondary branching, whereas the sample fabricated with no preheating of the plate presents a smaller grain size and fine dendrites with no secondary branching. Grain size and dendrite size will be discussed in section 3.2.3.

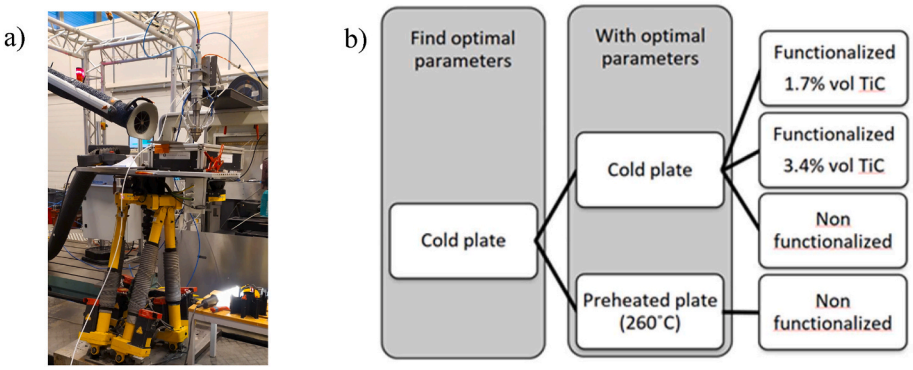

Fig. 2. Images of a) Laser DED system set-up and b) flow chart of the experimental procedure.

Table 3
Specimens subjected to post-heat treatment.

Group	No. samples	Laser power (W)	Travel speed (mm/s)	Powder feed rate (g/min)	No. layers	Preheat	Powder
A	2	1000	16.7	1.6	50	No	7075
B	2	1000	16.7	1.6	50	Yes	7075
C	2	1000	16.7	1.6	50	No	7075 + 1.7% TiC
D	2	1000	16.7	1.6	50	No	7075 + 3.4% TiC

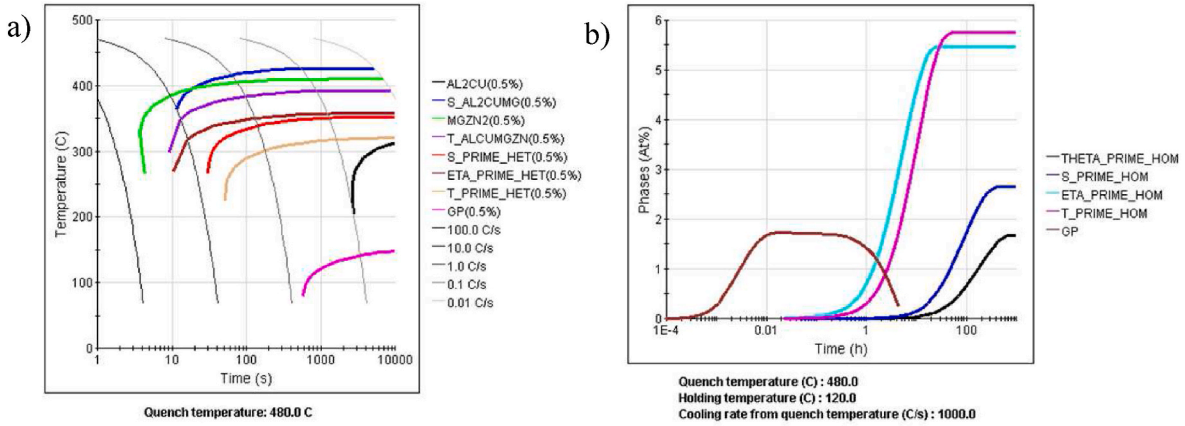

Fig. 3. Diagrams of a) CCT and b) isothermal precipitation kinetics calculated by JMatPro using original powder feedstock composition.

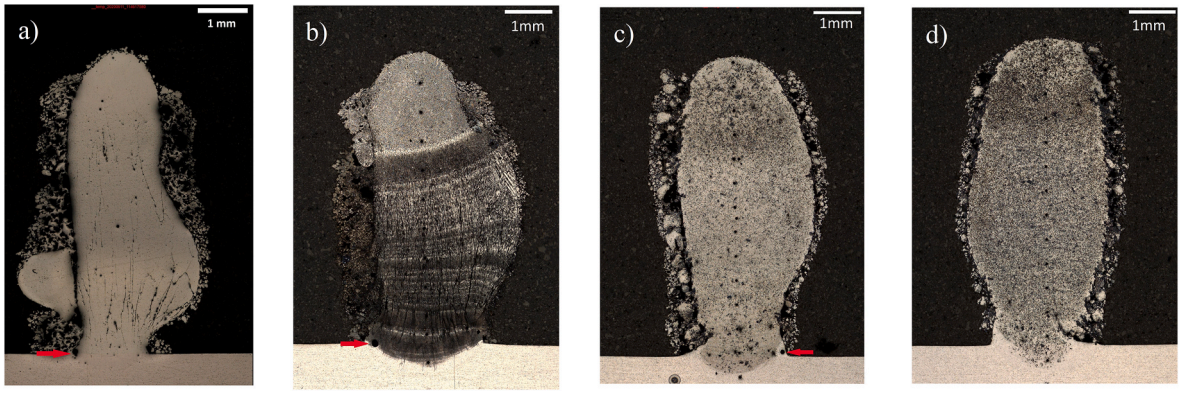

Fig. 4. Cross-sections of as-built samples processed with optimum parameters a) on a cold plate, b) on a preheated plate, c) with 1.7% TiC, d) with 3.4% TiC. All samples have 50 layers.

There is an absence of cracks on samples c and d from Fig. 4, and the microstructure is uniform in all the cross-sections. It presents fine equiaxed grains and the absence of dendrites. The sample also has spotted appearance where the dark spots are made of TiC. Fig. 5e and f shows the dark spots in detail, where samples with a higher TiC concentration present more dark areas.

3.1.1. Cracks

It can be observed, from samples a and b in Fig. 4, that cracks grow as the number of layers increases; however, cracks are not present in the last layer. As discussed previously, they are visible only in the layers beneath the last one. Moreover, cracks were suppressed with the addition of TiC. These cracks can have two origins: residual stresses and hot cracking. It is important to consider aluminum's high coefficient of thermal expansion, as the dimensional changes when it is heated or cooled down produce distortions and residual stresses, which can produce cracks, as already mentioned [4,23–27].

Distortions and residual stresses are not produced when the temperature distribution is uniform and there is no external restraint. In welding, preheating the base material can solve this problem [23,24,26,27]. Cracks are still present on the samples when they are fabricated on a preheated build plate, which means that distortions and residual stresses were not the leading cause of cracks. The most probable cause for the appearance of cracks is due to hot cracking, as 7075 contains low melting point elements and components such as Zn and Al–Cu components.

The dendrites grow as the melt cools down and segregates lower melting point and other elements towards the solidification front, which becomes entrapped between the dendrites. This stage is the most susceptible to hot cracking, as explained in Ref. [28]. In the end, when there is no more liquid flow into these interdendritic areas, the low melting point elements solidify and contract, creating voids and cracks [4,22,28]. When dendrites continue growing, if they have the same crystallographic orientation, the dendrite branches are coherent with each other and coalesce, creating a bridge that unites different dendrites. Dendrite coherency presents a high resistance to strains making it less susceptible to hot cracking. Samples that present cracks also have areas with coherent dendrites [22,28].

However, grain boundaries are highly susceptible to hot cracking, as they present a high-energy planar interface that liquid can fill. First, there is no dendrite coherency and no interdendritic bridging, so a dendrite boundary appears, where segregation of low melting point and other elements occurs. Secondly, grain boundaries make crack propagation easy. And thirdly, the structure is affected by dendrite morphology oriented towards the building direction in the samples, explaining why the cracks are oriented in this direction [26,28]. In addition, an investigation performed by EBSD (Fig. 6) confirmed that non-functionalized samples have large elongated grains that grow towards the building direction and cracks, displayed in detail in SEM micrographs (Fig. 7), coincide with the grain boundaries, indicating intergranular fracture. It shows that the fracture surface does not present a dendritic morphology, which may suggest that the cracks result from an intergranular fracture due to the presence of a liquid component. This finding verifies the explanation of the results discussed in the previous paragraph. These features are characteristic of liquation cracking which is a hot cracking phenomenon. Liquation cracking occurs in the partially melted zone (PMZ), where the material overpasses the eutectic temperature. Hence, the low melting point elements segregated on the grain

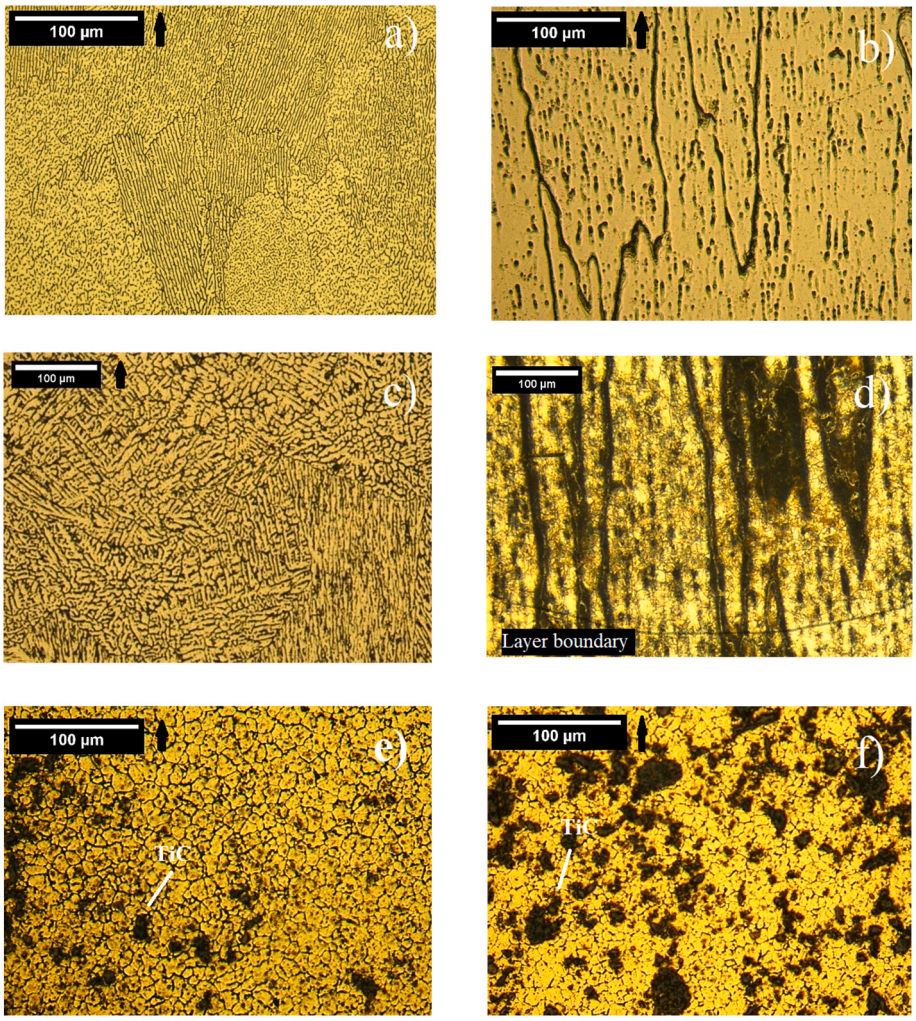

Fig. 5. Cross-sections of samples made with optimal parameters at a higher magnification where a) upper part and b) crack area of sample built on a cold plate, c) upper part and d) crack area of sample built on a preheated plate, e) sample made with 1.7% TiC, f) sample made with 3.4% TiC. The arrow next to the scale bar indicates the building direction.

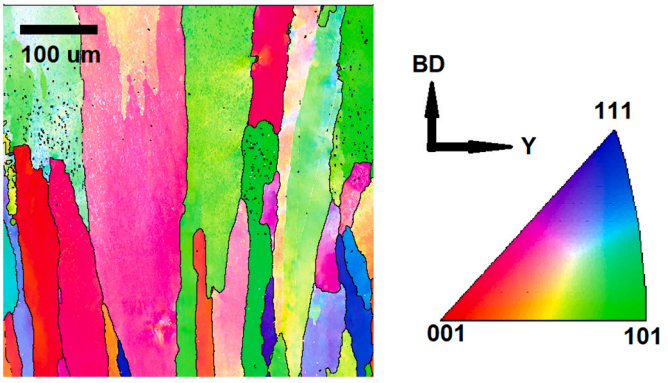

Fig. 6. EBSD inverse pole figure (IPF) orientation maps of non-functionalized AA7075 sample built on a cold plate. BD represents the building direction.

boundaries become liquid. The grain boundary becomes weak and fractures when this liquid zone solidifies and contracts [29]. This explanation clarifies why the last layer of the material does not crack, as it is not subjected to another thermal cycle where a PMZ forms, but the metal of the layers underneath does.

EDS results (as shown in Table 4) show on both samples (Fig. 7) a significant amount of Cu on the crack surface, 10% on average, whereas, in the adjacent areas, there seems to be much less Cu. Copper has a very high melting point but forms low melting compounds in the Al–Mg–Cu system [28]. Due to the low melting compounds, there is segregation of the Al_2CuMg phase on the solidification front during solidification. Segregation of Cu components, especially Al_2CuMg from dendrite and grain boundaries, causes hot cracking on 7075 alloy [3,28,30,31]. This coincides with the results from Bhagavatam et al. and Sokoluk et al. [3, 6].

There was also a slightly higher concentration of Zn on the crack surface than on the free defect surface. The concentration on the crack, measured with EDS, was around 6% whereas Zn distribution was homogeneous on the rest of the sample with a concentration of ~3% in non-functionalized samples. These differences in concentration indicate that Zn segregation has also been on dendrites and grain boundaries, an element with a low melting point.

The AA7075 powder contains 5.2 wt% of Zn, and the samples' content indicates a Zn loss of 42% regardless of the bed temperature. A study by Stopyra et al. [32] about AA7075 additive manufacturing with laser powder bed fusion (LPBF) showed a Zn loss of 23% and 30% when the laser power was 200 and 500 W, respectively. With DED, there is a 42% Zn loss when the laser power is 1000 W. The comparison of these values suggests a linear correlation between the Zn loss and the laser power.

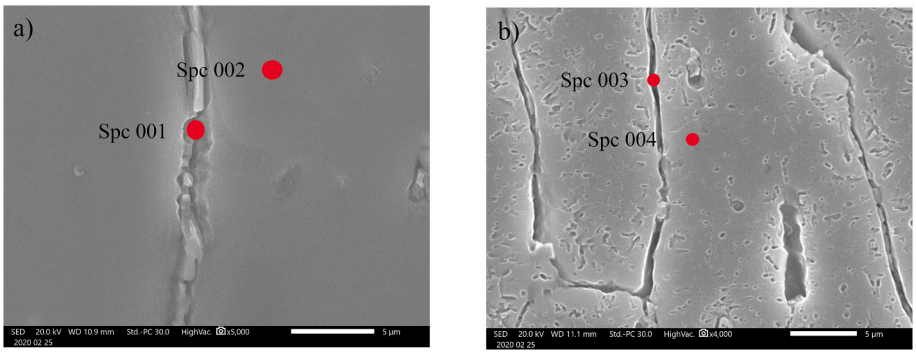

Fig. 7. SEM micrographs of cracks in samples made of non-functionalized powder on a) a cold plate, b) a preheated plate.

Table 4
EDS results in wt.%.

Location	Al	Cu	Zn
Spc 001	83.2 ± 0.6	10.4 ± 0.4	6.4 ± 0.4
Spc 002	95.9 ± 0.5	0.9 ± 0.1	3.2 ± 0.2
Spc 003	84.0 ± 0.7	10.4 ± 0.5	5.7 ± 0.4
Spc 004	96.8 ± 0.5	0.5 ± 0.1	2.8 ± 0.2

Hot cracking is suppressed with the addition of TiC, as seen in Fig. 4c and d. TiC acts as a nucleation enhancer, promoting heterogeneous nucleation, which stops the formation of columnar dendrites and produces fine equiaxed grains, as seen in Fig. 5e and f. As discussed earlier, heterogeneous nucleation occurs when there is a reduction in interfacial energy, which is favorable when there is good contact between the solid surface and liquid. This is the effect TiC nanoparticles have over the molten aluminum, as TiC has a lattice mismatch factor of 5.8% with aluminum. This means that aluminum nucleates easily on the surface of the nanoparticles, as it reduces the interfacial energy and nucleation barrier [5–7,33]. Similar results have been reported by Bhagavatam et al. and Sokoluk et al. [3,6].

3.1.2. Porosity

In general, the samples had low porosity. The measured values represent only 0.002–0.161% of the total area of the samples. Pores in the samples present two different morphologies. The pores on the sample's edges have an irregular shape, whereas the pores inside the sample have a spherical shape. The first morphology is associated with improper melting [34]. Spherical pores are associated with bubbles of evaporated elements entrapped in the melt pool [3,4,34]. Magnesium and especially Zinc have low boiling points, which can explain the morphology of these pores. The most characteristic pores that appear in

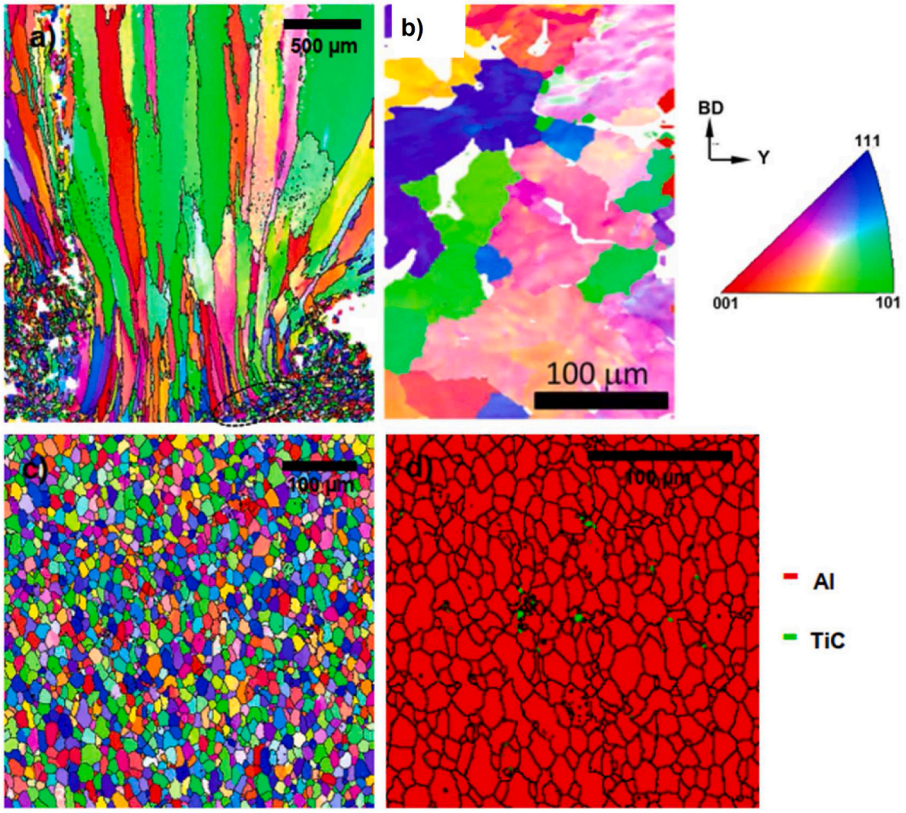

Fig. 8. EBSD IPF orientation (a, b, c) and phase maps (d) of a) non-functionalized AA7075 sample built on a cold plate, b) as-cast AA7075 [35], c) functionalized AA7075 sample subjected to 24 h-T6 and d) functionalized AA7075 sample subjected to 24 h-T6, where green represents TiC and red Al. The color code is only valid for figures a and c.

almost all the samples are single big rounded shaped pores of 50–100 μm in diameter on the bottom of the sample, next to the building plate, like the ones seen in Fig. 4a, b, and c highlighted by a red arrow. EDS results show high concentrations of Zn on the surface of these pores, which indicates that it has evaporated and entrapped in the melt pool.

3.1.3. Grain size and morphology

Samples printed on a cold plate with non-functionalized powders revealed irregularly shaped grains of 93 μm of average size on the top of the sample, which corresponded to the last layer and exhibited primary dendrites with a columnar structure (see Fig. 5a). Furthermore, the bottom area, corresponding to the layers underneath the top one, shows large irregular elongated grains growing towards the building direction, as illustrated in Figs. 6 and 8a. The average grain size is difficult to measure, as they have a wide variation in lengths and thicknesses, but, as seen in Fig. 8a, the smaller grains, which correspond to the first layers are around 500 μm long. In contrast, the upper layers form larger grains exceeding 1 mm in length. Epitaxial growth explains why there is no discontinuity showing layers on the grain structure, and there are, instead, largely elongated that comprehend several layers. Furthermore, from Fig. 8a, a predominant crystallographic grain orientation is visible. Mostly {101}, but there are grains with {001} orientation, too. The base has smaller grains with less orientation when compared to the upper grains, which have orientations between {001} – {101} and {001} – {111}. The base plate material has small grains randomly oriented, which probably affects the orientation of the first deposited layer.

Samples built with non-functionalized powders on the preheated plate exhibit irregularly shaped grains with an average size of 221 μm on the top of the sample. The microstructure consists of coarse dendrites with secondary branching (Fig. 5c). These microstructures are typical for pure as-cast AA7075 after various cooling rates [17]. Fig. 8b shows an IPF orientation map of a typical as-cast AA7075 microstructure, where the grains are irregular with randomly oriented equiaxed grains.

The samples built on the preheated plate are subjected to slower cooling rates than the ones made on a cold plate. High cooling rates at the solidification stage enhance the driving force and produce more nuclei than slow cooling rates. For this reason, the cooling rate influences dendritic and grain growth during solidification. As they are diffusion-controlled mechanisms, they are thermally activated processes that require a certain amount of energy and time to occur. High cooling rates inhibit diffusion and the driving force for solidification increases. There is less time for diffusion, which results in finer microstructures [17,33,36–38].

As discussed in previous sections, adding TiC plays an essential role in grain size and morphology. Microstructures contained fine equiaxed grains with an average size of 11.5 μm and 9.7 μm when the amount of TiC was 1.7% and 3.4%, respectively. These samples did not present dendritic structures. These results coincide with the studies made by Sokoluk et al. [6,17]. Besides grain refinement and growth restriction, nanoparticle additions modify secondary phases and increase the amount of liquid phase at the terminal stage of solidification as reported recently by Sokoluk et al. [39].

However, TiC was not homogeneously dispersed in the Al matrix; instead, it formed clusters, as seen in Fig. 5e and f, and confirmed in Fig. 8d, where the green areas represent TiC agglomeration. It seems that adding more nucleation enhancers refined the structures more, but the refinement was not very significant with those concentrations used in the present study. In addition, samples having 3.4% TiC showed larger agglomerations than the samples made with 1.7% TiC. Other studies observed similar behavior on the influence of the addition of various concentrations of nucleation enhancers, such as TiC, Al_2O_3, SiC, and TiB_2 on the AA7075 matrix [12,14,15,40].

3.1.4. Melt pool, HAZ, and layers

The samples were fabricated layer by layer by a single laser track, so each layer was composed of one single melt pool. This is visible in Fig. 4b. In addition, samples made with non-functionalized powders show a top part that measures around 1,5 mm height on average and a cracked area with a directional dendritic growth towards the building direction. The layered structure results from overlapping melting pools, and the top part corresponds to the last melting pool. The final layer does not overlap and has a structure that resembles the as-cast one.

When the material is deposited and melted on the base plate, it nucleates following the same structural orientation as the base material and grows following the thermal gradient. In addition, with the deposition of the subsequent layers, the grains grow following the same structural orientation [41]. This is called epitaxial growth, which gives AM microstructures the characteristic outlook. A typical AM microstructure is presented in Fig. 8a. However, on the last melt pool, epitaxial growth is lost near the top edge, as the cooling rate is higher at the top of the melt pool. On the contrary, the bottom of the melt pool is the one with the lowest cooling rate, producing coarse dendritic structures at the melt pool boundaries [42] as seen in Fig. 5d. Epitaxial growth towards the building direction is a possible explanation for the cracks appearing parallel to the building direction.

3.2. Hardness

From Fig. 9, it is clear that hardness is not uniform across the sample. There are three hardness zones in both 10 and 50 layered samples. The top zone presents an average hardness of 70 HV. In the middle zone, the hardness increases, reaching values of 85–90 HV, and finally, there is a drop of hardness on the bottom of the sample to values around 65 HV.

Hardness values of AA7075 fabricated with AM and without T6 treatment were lower than those of the as-cast state. However, these results are in line with those Sun et al. [43] obtained. They explained the low hardness by the formation of segregation structures in the grain boundaries during solidification in the PBF process. The Cu segregation found on the grain boundary cracks also indicates that this may be the case in the present study.

Except for the presence of Cu on the crack surfaces, EDS analysis shows no abnormalities in composition between the top part of the sample and the cracked area, so the increase in hardness on the cracked area is not related to the elemental alloying difference between the top and the rest of the sample.

One possible explanation for the hardness increase when moving away from the top part of the sample is interdendritic bridging. Dendrite coherency presents a high resistance to strains, which means that this microstructure has developed considerable strength. The area that showed higher hardness than the top coincides with interdendritic bonding, which explains this hardness increase [22]. However, this theory does not explain the behavior of the samples including TiC.

Even if TiC-containing samples did not have cracks, residual stresses were formed. The formation of residual stresses is very common during welding and AM processes due to the high cooling rates, thermal gradients, and high thermal expansion of aluminum [44]. In addition, the material at the bottom part has been subjected to a higher number of thermal cycles than the top one, which may increase distortions and residual stresses in that area. On the other hand, layers have been deposited on a cold substrate of a dissimilar aluminum alloy, it is more susceptible to residual stresses. Residual stresses have an essential role in hardness, as they distort the lattice [4,23–27]. This can explain the increase in hardness in both functionalized and non-functionalized samples. The micrographs in Fig. 10 confirm that local misorientations indicate residual stresses. Besides, these misorientations are concentrated in a band-like area perpendicular to the building direction, which may be related to the thermal history of the material during the sample's fabrication by layers.

Apart from dendrite coherency and residual stresses, another reason for the increase in hardness can be the thermal cycles during the building process. The material was subjected to several complex thermal cycles as it was built layer by layer. It was subjected to melting and

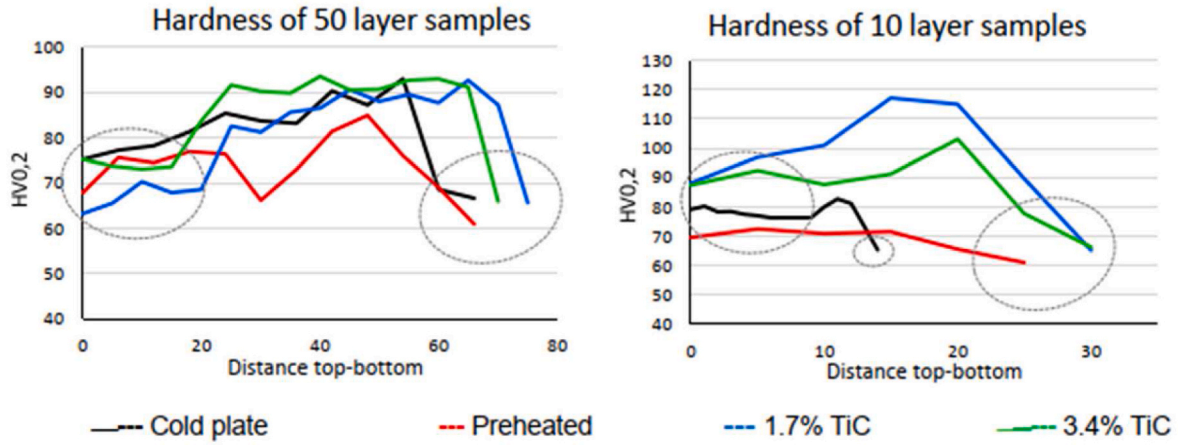

Fig. 9. Hardness of cross sections of 50 and 10 layered samples. Circles indicate the top of the sample and base plate.

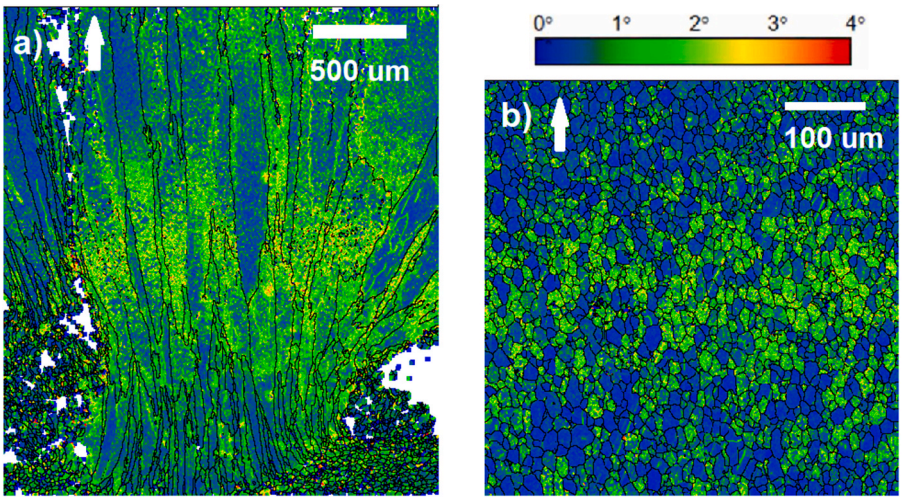

Fig. 10. EBSD local misorientation maps of a) non-functionalized AA7075 sample built on a cold plate and b) functionalized AA7075 sample subjected to 24 h-T6. Color represents local misorientation angles. The arrows represent the building direction.

reheating that heat-treated metal, producing phase transformations by the subsequent beads [45,46]. In the case of AA7075, these heat treatments can lead to precipitation of hardening phases, such as $MgZn_2$. Some studies show that precipitation hardening takes place in age-hardenable alloys (maraging steels, Al–Sc alloys, and Ni-base superalloys) while components are produced by AM [45,46].

The hardness drop in the bottom is due to dilution caused by the base plate (around 60 HV) [47]. The HAZ hardness showed transition values from 90 to 60 HV, as seen in the selected values of Fig. 9. In general, the hardness values are slightly higher in samples having TiC additions because TiC increases the hardness of 7075 [6,17,48,49]. In addition, in TiC agglomerations hardness was overpassing 100 HV.

3.3. Thermal post-processing

3.3.1. Microstructure analysis

When common aluminum alloys, such as AA7075, are heat-treated and the temperature exceeds 455 °C, there can be recrystallization and/or grain growth problems [50]. Besides, there are reports of grain growth at temperatures as low as 345 °C [50]. For this reason, it is expected to have some grain growth in the T6 heat-treated samples as they have been subjected to 480 °C during solution annealing.

Fig. 11a presents the columnar dendritic structure of the top of a sample made with non-functionalized powders and built on a cold plate. The average primary dendrite arm spacing is 7.6 μm, whereas, without T6 treatment (Fig. 5a), it was 2.6 μm, meaning that the dendritic spacing has grown almost three times. In addition, the grains reached an average size of 234 μm, which is also three times the grain size before the T6 treatment. In Fig. 11b, the columnar coherent dendritic structure of a non-functionalized sample shows small voids and cracks that are also present in the non-heat-treated samples.

$MgZn_2$ precipitates precipitate on the grain boundaries of T6 treated samples, but they are not visible with optical microscopy due to their small size [6,51–53].

Samples made with functionalized powders present a more noticeable microstructural change. The upper part of the sample remains unchanged, with an average grain size of 7 μm, as shown in Fig. 11c for 3.4% TiC addition, which is the same magnitude as in the functionalized samples without T6 treatment. However, the microstructure suggests a gradual change as it becomes closer to the first deposited layer. The microstructural evolution at the bottom of the samples is more noticeable (Fig. 11c). It looks like the grains have grown towards the building direction. In Fig. 8d, grains show a preferential growth orientation. The grains at the bottom have an average size of 12.7 μm (Fig. 8c).

3.3.2. Hardness

T6 heat-treated samples show a hardness value of 110HV (Fig. 12), which is below the standard requirement. This result coincides with the

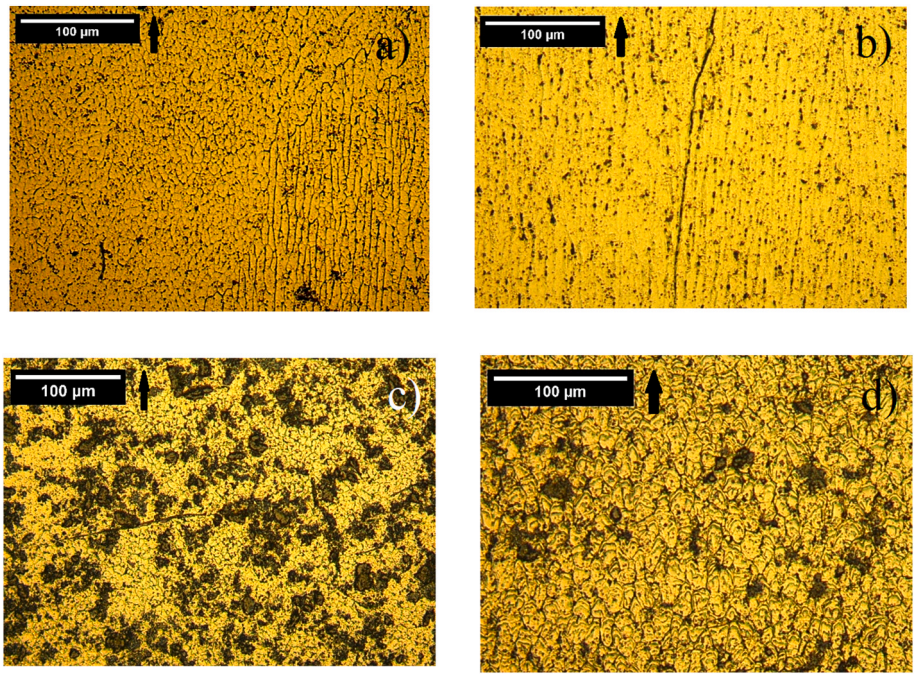

Fig. 11. Microstructures after heat treatment a) top and b) bottom of non-functionalized samples built on a cold plate after 24 h of aging, c) top with 3.4% TiC after 21 h, and d) bottom with 1.7% TiC after 21 h. The arrow represents the building direction.

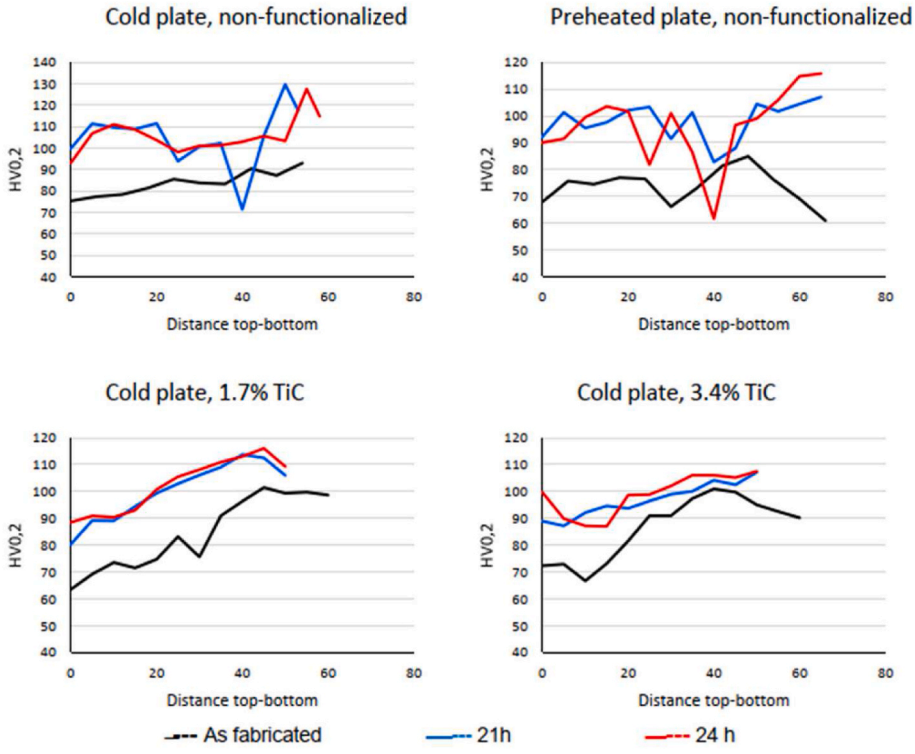

Fig. 12. Hardness values of four different samples as-fabricated (black), after aging for 21 h (blue) and 24 h (red).

results obtained by Bhagavatam et al. [3] and states that the low hardness is the result of the evaporation of Zn. Consequently, the reduction of Zn content decreases the amount of $MgZn_2$ precipitates. Another possible explanation for low hardness values after heat treatment is an inadequate aging response from the complex thermal cycles that may have induced over-aging. There are studies where AlSi10Mg alloy processed by PBF did not respond adequately to T6 temper, presenting lower mechanical strength than expected due to the explained problem [54]. Although there was a scatter in the hardness values across the cross-section, the values after 21 h and 24 h aging were very similar. The samples made on a cold plate with non-functionalized powders have lower hardness levels in the middle part of the sample.

In contrast, the upper part has higher values, which is the opposite behavior of the one presented by the non-heat-treated samples. This

finding can mean that the lower layers may have been overaged due to the sample's thermal history, whereas the top part may have been subjected to a proper aging treatment. The same occurs in the samples made on a preheated plate, where there was a clear drop in hardness after the heat treatment in the area where there was a hardness peak in the non-heat-treated samples.

On the other hand, the functionalized samples show a linear hardness increase towards the bottom of the samples, presenting the same behavior as the non-heat-treated samples. This observation indicates that the hardness of the upper part can still increase. In addition, this behavior can also be related to the residual stresses that remain after the heat treatment, as seen in Fig. 10b. Residual stresses are present in aluminum alloys subjected to precipitation hardening as T6 tempers only provide a slight reduction in stresses, in the range of 10–35% of the yield strength [50].

4. Conclusions

High strength AA7075 is functionalized with TiC nanoparticles to see if these nucleation enhancers can improve the printability of the alloy by suppressing hot cracking, how the addition of these nanoparticles influence on the microstructure of the aluminum alloy, and if it is in general possible to additively manufacture AA7075 with DED.

The segregation of Al_2CuMg produces hot cracks on the grain boundaries in the non-functionalized samples. Although porosity in the samples is low, the evaporation and entrapment of Zn on the melt pool causes large single pores on the base of the samples. In addition, it compromises the mechanical properties of the alloy.

Even though T6 heat-treated samples show a hardness increase, the values do not reach the standard's requirements due to possible evaporation of Zn and over-aging.

The addition of TiC successfully solves the hot cracking problem on AA7075 by inhibiting dendritic growth, obtaining fine equiaxed grains, suppressing hot cracking, and enhancing the printability of the material. However, the distribution of TiC is not homogeneous through the Al matrix but is present in clusters.

TiC nanoparticles enhance the printability of AA7075 due to hot cracking suppression. Furthermore, functionalized samples present refined equiaxed grains instead of large elongated grains oriented towards the building direction with a dendritic structure. However, to correctly print AA7075 with DED, it is necessary to develop a method to suppress or at least reduce Zn evaporation.

Credit author statement

Lucia Cobian Gonzalez Conducting a research & performing experiments (Investigation), **Jari Tuominen** Reviewing the manuscript (Writing – Review & Editing), **Shahroz Ahmed** Conducting a research & performing experiments (Investigation), **Madan Patnamsetty** Conducting a research & performing experiments (Investigation), **Pasi Peura** Oversight and leadership (Supervision).

Declaration of competing interest

The authors declare that they have no known competing financial interests or personal relationships that could have appeared to influence the work reported in this paper.

Data availability

Data will be made available on request.

References

[1] E.T.F. Trends, Why Investments in Additive Manufacturing Are Likely to Increase in 2020, 2019. https://www.etftrends.com/thematic-investing-channel/why-investments-in-additive-manufacturing-are-likely-to-increase-in-2020/. (Accessed October 2019). accessed.

[2] N. Li, S. Huang, G. Zhang, R. Qin, W. Liu, H. Xiong, G. Shi, J. Blackburn, Progress in additive manufacturing on new materials: a review, J. Mater. Sci. Technol. 35 (2019) 242–269, https://doi.org/10.1016/j.jmst.2018.09.002.

[3] A. Bhagavatam, A. Ramakrishnan, V.S.K. Adapa, G.P. Dinda, Laser metal deposition of aluminum 7075 alloy, Int J Mater Sci Res 2 (2018) 50–55, https://doi.org/10.18689/ijmsr-1000108.

[4] G. Mathers, The Welding Aluminium and its Alloys, first ed., CRC Press LLC, Boca Raton, 2002.

[5] J.H. Martin, B.D. Yahata, J.M. Hundley, J.A. Mayer, T.A. Schaedler, T.M. Pollock, 3D printing of high-strength aluminium alloys, Nature 549 (2017) 365–369, https://doi.org/10.1038/nature23894.

[6] M. Sokoluk, C. Cao, S. Pan, X. Li, Nanoparticle-enabled phase control for arc welding of unweldable aluminum alloy 7075, Nat. Commun. 10 (2019) 1–8, https://doi.org/10.1038/s41467-018-07989-y.

[7] K.T. Kashyap, T. Chandrashekar, Effects and mechanisms of grain refinement in aluminium alloys, Bull. Mater. Sci. 24 (2001) 345–353, https://doi.org/10.1007/BF02708630.

[8] P.S. Mohanty, J.E. Gruzleski, Mechanism of grain refinement in aluminium, Acta Metall. Mater. 43 (1995) 2001–2012, https://doi.org/10.1016/0956-7151(94)00405-7.

[9] C.E.S. EduPack, Granta Design Ltd, Cambridge, United Kingdom), 2018.

[10] F.A. Crossley, L.F. Mondolfo, Mechanism of grain refinement in aluminum alloys, JOM (J. Occup. Med.) 3 (1951) 1143–1148, https://doi.org/10.1007/BF03397424.

[11] A.F. Norman, K. Hyde, F. Costello, S. Thompson, S. Birley, P.B. Parangnell, Examination of the effect of Sc on 2000 and 7000 series aluminium alloy castings: for improvements in fusion welding, Mater. Sci. Eng., A 354 (2003) 188–198, https://doi.org/10.1016/S0921-5093(02)00942-5.

[12] R.R. Veeravalli, R. Nallu, S.M.M. Mohiuddin, Mechanical and tribological properties of AA7075–TiC metal matrix composites under heat treated (T6) and cast conditions, J. Mater. Res. Technol. 5 (2016) 377–383, https://doi.org/10.1016/j.jmrt.2016.03.011.

[13] X.H. Chen, H. Yan, Solid-liquid interface dynamics during solidification of Al 7075-Al2O3np based metal matrix composites, Mater. Des. 94 (2016) 148–158, https://doi.org/10.1016/j.matdes.2016.01.042.

[14] C. Kannan, R. Ramanujam, Comparative study of the mechanical and microstructural characterisation of AA 7075 nano and hybrid nanocomposites produced by stir and squeeze casting, J. Adv. Res. 8 (2017) 309–318, https://doi.org/10.1016/j.jare.2017.02.005.

[15] W. Ruirui, Y. Zheng, L. Qiushu, Microstructure and mechanical properties of 7075 Al alloy based composites with Al_2O_3 nanoparticles, Int. J. Cast Metals Res. 30 (2017) 337–340, https://doi.org/10.1080/13640461.2017.1316954.

[16] A. Ghosh, M. Ghosh, G. Shankar, On the role of precipitates in controlling microstructure and mechanical properties of Ag and Sn added 7075 alloys during artificial ageing, Mater. Sci. Eng., A 738 (2018) 399–411, https://doi.org/10.1016/j.msea.2018.09.109.

[17] M. Zuo, M. Sokoluk, C. Cao, J. Yuan, S. Zeng, X. Li, Microstructure control and performance evolution of aluminum alloy 7075 by nano-treating, Sci. Rep. 9 (2019) 1–11, https://doi.org/10.1038/s41598-019-47182-9.

[18] J.H. Martin, B.D. Yahata, E.C. Clough, Recent advances in additive manufacturing of high strength 7000 series aluminum, Adv. Mater. Process. 176 (2018) 18–22.

[19] Samueli Newsroom, Nanotechnology Enables Engineers to Weld Previously Unweldable Aluminum Alloy, UCLA Samueli School of Engineering, 2019.

[20] X.P. Li, G. Jib, Z. Chen, A. Addad, Y. Wu, H.W. Wang, Selective laser melting of nano- TiB2 decorated AlSi10Mg alloy with high fracture strength and ductility, Acta Mater. 129 (2017) 183–193, https://doi.org/10.1016/j.actamat.2017.02.062.

[21] Z. Lei, J. Bi, Y. Chen, Effect of energy density on formability, microstructure and micro-hardness of selective laser melted Sc- and Zr- modified 7075 aluminum alloy, Powder Technol. 356 (2019) 594–606, https://doi.org/10.1016/j.powtec.2019.08.082.

[22] M.S. Fernandes de Lima, Phase transformations during laser processing of aerospace metallic materials, Adv. Mater. Res. 1135 (2016) 179–201. https://dx.doi.org/10.4028/www.scientific.net/AMR.1135.179.

[23] S. Kou, Welding Metallurgy, second ed., A John Wiley & Sons, Hoboken, 2003.

[24] F.C. Campbell, Joining: Understanding the Basics, first ed., ASM International®, Materials Park, 2011.

[25] J.M. Sánchez Amaya, M.R. Amaya-Vázquez, F.J. Botana, Ch.8 Laser welding of light metal alloys: aluminium and titanium alloys, in: S. Katayama (Ed.), Handbook of Laser Welding Technologies, Woodhead Publishing, 2013, pp. 215–254.

[26] S. Katayama, Ch 12, Defect formation mechanisms and preventive procedures in laser welding, in: S. Katayama (Ed.), Handbook of Laser Welding Technologies, Woodhead Publishing, 2013, pp. 332–373.

[27] H. Murakawa, Ch.13 Residual stress and distortion in laser welding, in: S. Katayama (Ed.), Handbook of Laser Welding Technologies, Woodhead Publishing, 2013, pp. 374–400.

[28] C. Cross, On the origin of weld solidification cracking, in: T. Böllinghaus, H. Herold (Eds.), Hot Cracking Phenomena in Welds, Springer, Berlin, 2005, p. 15.

[29] S. Kou, Solidification and liquation cracking issues in welding, JOM (J. Occup. Med.) 55 (2003) 37–42, https://doi.org/10.1007/s11837-003-0137-4.

[30] C.M. Cheng, C.P. Chou, I.K. Lee, H.Y. Lin, Hot cracking of welds on heat treatable aluminium alloys, Sci. Technol. Weld. Join. 10 (2013) 344–352, https://doi.org/10.1179/174329305X40688.

[31] C. Huang, S. Kou, Liquation mechanisms in multicomponent aluminum alloys during welding, Weld. J. 81 (2002) 211–222.

[32] W. Stopyra, K. Gruber, I. Smolina, T. Kurzynowski, B. Kuźnicka, Laser powder bed fusion of AA7075 alloy: influence of process parameters on porosity and hot cracking, Addit. Manuf. 35 (2020), 101270, https://doi.org/10.1016/j.addma.2020.101270.
[33] D. Porter, K. Easterling, M. Sherif, Phase Transformations in Metals and Alloys, third ed., Taylor & Francis Group, Boca Raton, 2009.
[34] Z. Eddie Tan, J.H. Lye Pang, J. Kaminiski, J.H. Pepin, Characterisation of porosity, density, and microstructure of directed energy deposited stainless steel AISI 316L, Addit. Manuf. 25 (2019) 289–296, https://doi.org/10.1016/j.addma.2018.11.014.
[35] K.R. Ramkumar, S. Sivasankaran, F.A. Al-Mufadi, S. Siddharth, R. Raghu, Investigations on microstructure, mechanical and tribological behaviour of AA 7075-x wt.% TiC composites for aerospace applications, Arch. Civ. Mech. Eng. 19 (2019) 428–438, https://doi.org/10.1016/j.acme.2018.12.003.
[36] K.H.W. Seah, J. Hemanth, S.C. Sharma, Effect of the cooling rate on the dendrite arm spacing and the ultimate tensile strength of cast iron, J. Mater. Sci. 33 (1998) 23–28, https://doi.org/10.1023/A:1004321007806.
[37] P. Feltham, Grain growth in metals, Acta Metall. 5 (1957) 97–105, https://doi.org/10.1016/0001-6160(57)90136-0.
[38] P. Peng, X. Li, J. Li, Y. Su, J. Guo, H. Fu, Detachment of secondary dendrite arm in a directionally solidified Sn-Ni peritectic alloy under deceleration growth condition, Sci. Rep. 6 (2016) 1–12, https://doi.org/10.1038/srep27682.
[39] M. Sokoluk, J. Yuan, S. Pan, X. Li, Nanoparticles enabled mechanism for hot cracking elimination in aluminum alloy, Metall. Mater. Trans. 52A (2021) 3083–3096, https://doi.org/10.1007/s11661-021-06302-9.
[40] G. Gan, B. Yang, B. Zhang, X. Jiang, Y. Shi, Y. Wu, Refining mechanism of 7075 Al alloy by in-situ TiB_2 particles, Materials 10 (2017) 132–143, https://doi.org/10.3390/ma10020132.
[41] A. Basak, S. Das, Epitaxy and microstructure evolution in metal additive manufacturing, Annu. Rev. Mater. Res. 46 (2016) 125–149, https://doi.org/10.1146/annurev-matsci-070115-031728.
[42] Y.J. Liu, Z. Liu, Y. Jiang, G.W. Wang, Y. Yang, L.C. Zhang, Gradient in microstructure and mechanical property of selective laser melted AlSi10Mg, J. Alloys Compd. 735 (2018) 1414–1421, https://doi.org/10.1016/j.jallcom.2017.11.020.
[43] S. Sun, P. Liu, J. Hu, C. Hong, X. Quiao, S. Liu, R. Zhang, C. Wu, Effect of solid solution plus double aging on microstructural characterization of 7075 Al alloys fabricated by selective laser melting (SLM), Opt Laser. Technol. 114 (2019) 158–163, https://doi.org/10.1016/j.optlastec.2019.02.006.
[44] I. Gibson, D. Rosen, B. Stucker, Additive Manufacturing Technologies, first ed., Springer Science + Business Media, New York, 2015.
[45] D.D. Gu, W. Meiners, K. Wissenbach, R. Poprawe, Laser additive manufacturing of metallic components: materials, processes and mechanisms, Int. Mater. Rev. 57 (2012) 133–164, https://doi.org/10.1179/1743280411Y.0000000014.
[46] E.A. Jägle, Z. Sheng, L. Wu, L. Lu, J. Risse, A. Weisheit, D. Raabe, Precipitation reactions in age-hardenable alloys during laser additive manufacturing, JOM (J. Occup. Med.) 68 (2016) 943–949, https://doi.org/10.1007/s11837-015-1764-2.
[47] Aalco®, Aluminium Alloy 5754-H111 Treadplate.
[48] C. Li, S. Sun, C. Liu, Q. Lu, P. Ma, Y. Wang, Microstructure and mechanical properties of TiC/AlSi10Mg alloy fabricated by laser additive manufacturing under high-frequency micro-vibration, J. Alloys Compd. 794 (2019) 236–246, https://doi.org/10.1016/j.jallcom.2019.04.287.
[49] C. Li, S. Sun, Y. Zhang, C. Liu, P. Deng, M. Zeng, F. Wang, P. Ma, W. Li, Y. Wang, Effects of laser processing parameters on microstructure and mechanical properties of additively manufactured AlSi10Mg alloys reinforced by TiC, Int. J. Adv. Manuf. Technol. 103 (2019) 3235–3246, https://doi.org/10.1007/s00170-019-04001-9.
[50] ASM Handbook, in: first ed.Heat Treating, Heat Treating of Aluminum Alloys, ume 4, ASM International®, Materials Park, 1991, pp. 841–879, https://doi.org/10.1361/asmhba0001205.
[51] P.X. Zhang, H. Yan, W. Liu, X.L. Zou, B.B. Tang, Effect of T6 heat treatment on microstructure and hardness of nanosized Al_2O_3 reinforced 7075 aluminum matrix composites, Metals 9 (2019) 44–56, https://doi.org/10.3390/met9010044.
[52] A. Korbel, W. Bochniak, J. Borowski, J.L. Blaz, P. Ostachowski, M. Lagoda, Anomalies in precipitation hardening process of 7075 aluminum alloy by KOBO method, J. Mater. Process. Technol. 216 (2015) 160–168, https://doi.org/10.1016/j.jmatprotec.2014.09.008.
[53] N. Mahathaninwong, T. Plookphol, J. Wannasin, S. Wisutmethangoon, T6 heat treatment rheocasting 7075 Al alloy, Mater. Sci. Eng., A 532 (2012) 91–99, https://doi.org/10.1016/j.msea.2011.10.068.
[54] R. Casati, M.H. Nasab, M. Coduri, V. Tirelli, M. Vedani, Effects of platform preheating and thermal-treatment strategies on properties of AlSi10Mg alloy processed by selective laser melting, Metals 8 (2018) 954–966, https://doi.org/10.3390/met8110954.